

Understanding In-Plane Sliding of Functionalized $Ti_3C_2T_x$ MXene by In Situ Microscale Analysis of Electrochemical Actuation

Harpreet Singh, Shaohua Chen, Grégory Francius, Liang Liu,* Pooi See Lee, and Mathieu Etienne*



Cite This: *Chem. Mater.* 2024, 36, 9575–9583



Read Online

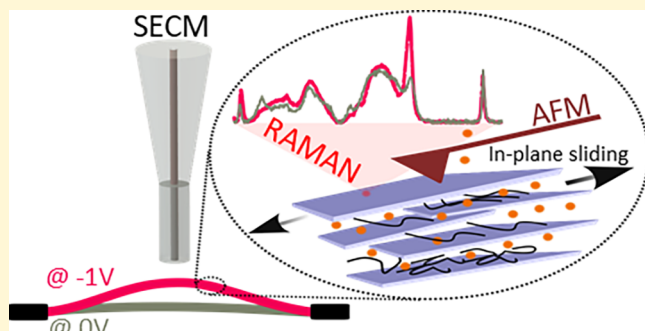
ACCESS |

Metrics & More

Article Recommendations

Supporting Information

ABSTRACT: Electrochemical actuation is based on the deformation of electrodes upon applying a mild potential (usually in the range of ± 5 V in a single cell). In this work, in situ local analysis of the electrochemical actuation of $Ti_3C_2T_x$ ($T = -O, -OH, -F$) MXene at the microscale is achieved by Raman spectroscopy, atomic force microscopy (AFM), and scanning electrochemical microscopy (SECM) while applying potential in an electrochemical cell. First, Raman spectra recorded at a steady state with different potentials confirm the intercalation/deintercalation of Li^+ ions, resulting in the change of out-of-plane vibrations due to the interaction of Li^+ with the $-O$ and $-OH$ surface group atoms of MXene. A methylcellulose functionalization of the MXene films results in more freedom for in-plane vibrations. Second, SECM is applied to visualize the deformation of two-end-fixed MXene films both at a steady state (0 V vs Ag/AgCl QRE) and at scanning potential. The results show buckling-type actuation, which is more pronounced for methylcellulose-functionalized samples. Electrochemical AFM provides evidence of a significant in-plane sliding of the MXene flakes. Out-of-plane changes appear to be negligible in the actuation mechanism, as supported by the AFM approach curve analysis. Overall, the methylcellulose-functionalized MXene shows better actuation performance, especially in the in-plane direction and at a high frequency. The mechanism is then discussed.



INTRODUCTION

Electrochemical actuators are based on the electrochemically induced deformation of electrodes, typically in a two-electrode configuration separated by an electrolyte layer. Compared with other types of actuators (electrical energy to mechanical energy,¹ magnetic field induced actuation,² spin transitions,³ magnetic field-dependent shape memory retention,⁴ piezoelectric mechanism,⁵ photoinduced molecular realignment,^{6–8} and thermally driven shape memory retention⁹), the electrochemical actuators are advantageous because of their compactness,¹⁰ lightweight, resistance to humidity in the case of ionic liquids¹¹ and corrosive¹² conditions, high deformation, and displacement under low-voltage applications.^{13,14} These advantages may significantly improve the safety of operation and reduce power consumption, which are suitable for various applications such as artificial muscles,^{15,16} flapping motions,¹⁷ tactile displays, bionics, switches, and converters.^{18–20}

Different active (or electrode) materials have been explored for electrochemical actuators, including graphene,^{21,22} carbon nanotubes,^{23–25} black phosphorus,²⁶ graphdiyne,²⁷ carbon nitride,²⁸ MOF,²⁹ MoS₂,³⁰ etc. Recently, MXene³¹ has shown a high potential as an electrode material for electrochemical actuators because of its high conductivity,³² flexibility,³³ and tunable interlayer spacing.³⁴ The material is easy to process, as it can form stable dispersions in various solvents including water. This colloidal solution can then be easily functionalized,

aligned, and stacked into layered film structures by following the simple vacuum filtration method.³⁵ Several types of MXenes (Ti_2CT_x ,³⁵ $Ti_3C_2T_x$,³⁶ Nb_2CT_x ,³⁷ $Nb_4C_3T_x$,^{38,39} V_2CT_x ,^{40–42} Mo_2CT_x ,⁴³ $Mo_4VC_4T_x$,⁴⁴ and $Mo_2Ti_2C_3$,⁴⁵) have been studied for energy storage applications.^{46–55} For the choice of electrochemical actuation, the capacitance, conductivity, and Young's modulus of the material are considered, and $Ti_3C_2T_x$ is selected as a suitable candidate for the application.

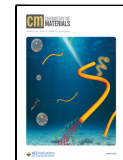
Various studies have demonstrated that the structure of MXene plays an important role in the actuation performance. This may further be improved by forming composites, such as with PEDOT:PSS/Ag nanowires⁵⁷ and polystyrene microspheres.⁵⁸ Recently, Chen et al. have reported the functionalization of MXene with methylcellulose and tetrabutylammonium for enhancing the electrochemical actuation performance.^{56,59} It is seen that a 15% functionalized film achieves a peak tensile strength of 53.2 MPa and a Young's modulus of

Received: June 7, 2024

Revised: September 12, 2024

Accepted: September 12, 2024

Published: October 1, 2024



over 10 GPa, surpassing many other materials like pure MC (0.3 MPa)⁶⁰ and PEDOT/MXene (23.3 MPa)⁶¹ films. The material is also mechanically robust under repeated folding.⁵⁶

Apart from the global strain analysis performed in the above-mentioned studies for the evaluation of actuation performance, *in situ* characterization methods are powerful tools for understanding the electrochemical behavior of MXene as an actuator electrode. Raman spectroscopy is widely used for probing the structural changes of electrodes during electrochemical reactions.^{62,63} It has also been used for studying an MXene/polypyrrole composite upon oxidation/reduction by following the changes on the C=C peak (1571 cm^{-1} : reduction state and 1607 cm^{-1} : oxidation state) of polypyrrole.⁶⁴ Scanning electrochemical microscopy (SECM) was originally proposed for imaging the topography of electrodes,⁶⁵ before it was more commonly used for studying the charge transfer kinetics.^{66,67} Topographic imaging by SECM was at the microscale, which was complemented by electrochemical atomic force microscopy (EC-AFM) and electrochemical scanning tunneling microscopy (EC-STM) with nanometer and atomic resolutions, respectively. Notably, SECM and EC-AFM may offer not only steady-state images of electrodes under a fixed applied potential but also the dynamic deformation and actuation in a potential scan. For example, Deng and coworkers⁶⁸ used EC-AFM to *in situ* study the formation of polycrystalline Pt during the cyclic voltammetry (CV) of a Pt electrode.

In this work, we attempt to carry out a comprehensive *in situ* study of the electrochemical actuation behavior of pristine and methylcellulose-functionalized MXene films. Raman spectroscopy is applied for analyzing the in-plane and out-of-plane vibrational modes of MXene upon applying the potential. SECM is used for quantifying the deformation of the MXene sample during actuation. EC-AFM is carried out for observing the in-plane sliding and out-of-plane expansion/contraction of MXene flakes. The obtained information provides a better understanding of the role of functionalization on the in-plane and out-of-plane actuation of MXene, which may guide the material optimization. Moreover, all the measurements reveal the actuation of MXene at the microscale. This may be helpful for designing MXene-based electrochemical actuator devices toward the desired directions of actuation.

■ EXPERIMENTAL METHODS

Materials Used. The synthesis of $\text{Ti}_3\text{C}_2\text{T}_x$ ($\text{T}_x = -\text{O}, -\text{OH}, -\text{F}$) MXene films with different weight contents of methylcellulose (0% (MX100MC00), 15% (MX85MC15), and 20% (MX80MC20)) is detailed in the Supporting Information.⁵⁶ The thickness of the films is ca. 30 μm as measured from profilometry (Figure S1a–c). 1,1'-Ferrocenedimethanol (purity 97%) and lithium sulfate (purity $\geq 98.5\%$) were purchased from Sigma-Aldrich for preparing the electrolyte solution with a concentration of 1 M lithium sulfate/1 mM 1,1'-ferrocenedimethanol. All of the other chemicals were of analytical grade and used without further purification. DI water was used as the solvent in all of the experiments.

Platinum wire (25 μm diameter, purity 99.9%, ChemPUR) and glass capillaries (Blaubrand intraMARK) were used for fabricating microelectrodes. The glass shield had a diameter of ca. 250 μm and an R_g (ratio between the radius of the insulation sheet and the radius of the conductive surface) of ~ 10 . The electrodes were polished to 4000 grits and cleaned by sonication in ethanol before use. The quality of the microelectrodes was ensured by measuring CV in 1 mM ferrocenedimethanol solution (Figure S2).

Electrochemical Cell. The electrochemical cell used for *in situ* studies of MXene was in a glass Petri dish (40 mm diameter, 12 mm

height) fixed by 3D-printed holders, with MXene sheets as the working electrode (WE), a Ag/AgCl wire as the quasi-reference electrode (QRE), and a carbon felt as the counter electrode (CE). The CE had a significantly larger surface area than the MXene WE. The electrolyte was 1 M Li_2SO_4 , and the potential was controlled using a PalmSens4 potentiostat in all measurements. The fixation of the MXene electrode, the addition of a second WE, and the redox mediator (ferrocenedimethanol) depend on the technique and thus will be described in detail later.

In Situ Raman Spectroscopy. The Raman analysis was performed in a three-electrode configuration (Figure 1a,d). The

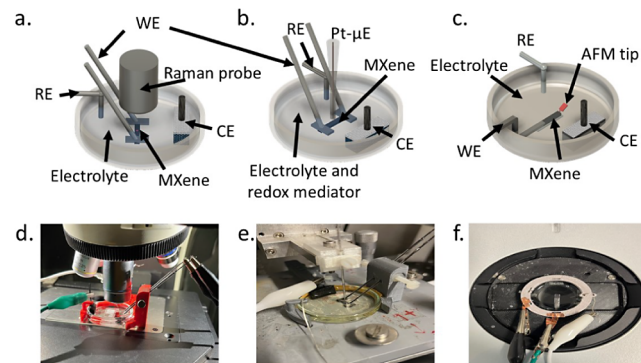


Figure 1. Schematic representations and images of the (a,d) Raman setup, (b,e) SECM setup, and (c,f) AFM setup. WE; working electrode, RE; reference electrode, CE; counter electrode, and Pt- μ E; platinum microelectrode.

MXene films were cut in strips of 2×10 mm, fixed by two carbon plates pressed by two carbon rods in short electrical connection, maintaining the exposed length of MXene at 5 mm. In this way, the MXene film can deform freely both in-plane and out-of-plane. The Raman spectra were recorded with a 785 nm excitation laser and an objective lens of L50 (N.A. 0.5) that showed all the vibrational modes related to the material (Figure S3a). The thickness of the electrolyte was maintained at ~ 1 mm, so that it was negligible as compared with the working distance of the objective lens (8 mm). Each spectrum was measured from 50 to 1400 cm^{-1} with an average of 12 scans with an exposure time of 12 s, which takes approximately 144 s. For this reason, the measurements were performed only at the steady state, i.e., at fixed potentials (0, -0.2 , -0.4 , -0.6 , -0.8 , and -1 V vs Ag/AgCl QRE). The spectral acquisition was started 200 s after switching the potential (Figure S3b), and the optical focus was readjusted following the actuation of the sample.

Scanning Electrochemical Microscopy (SECM). The SECM analysis was carried out in a four-electrode system (Figure 1b,e) in bipotentiostat mode. The MXene sample was fixed in the same way as for the Raman experiment, and 1 mM ferrocenedimethanol was added in the electrolyte as redox mediator. For approaching the Pt microelectrode to the MXene film, the microelectrode was connected as WE1 and poised at a fixed potential of 0.4 V vs Ag/AgCl QRE, and the MXene film was connected as WE2, biased at different potentials along the experiment (0, -0.5 , and -1 V vs Ag/AgCl QRE). The approach was stopped when the normalized current on WE1, as compared to that measured from bulk solution, reached 1.8 (no sample-tip touching condition). The lateral scan was performed between the two fixation points at an interval of 500 μm . At each sampling point, the microelectrode was approached from the same z position, and the stop position with the aforementioned criteria was recorded to retrieve the shape of the film. Furthermore, the transient deformation of MXene was measured with the film connected as WE1, and the microelectrode was connected as WE2. The potential of MXene (WE1) was scanned between 0 and -1 V vs Ag/AgCl QRE at 5 mV/s, while the potential of the Pt microelectrode (WE2) was maintained at 0.4 V vs Ag/AgCl QRE. The current response of both electrodes was recorded during the cycling.

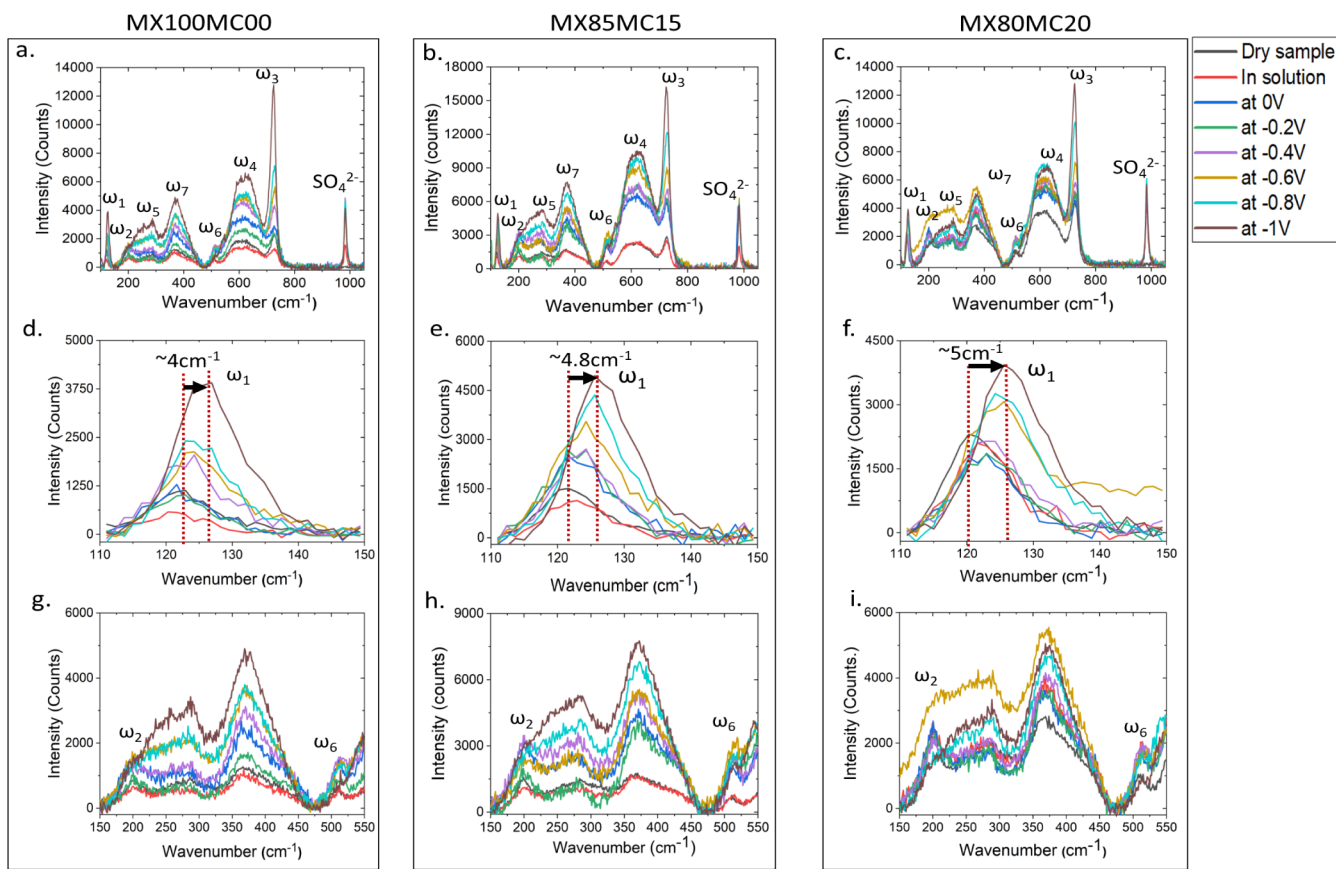


Figure 2. Full Raman spectra of $\text{Ti}_2\text{C}_3\text{T}_x$ at different applied potentials (0 to -1 V vs Ag/AgCl QRE) with (a) MX100MC00, (b) MX85MC15, and (c) MX80MC20. Zoom in the range of 110 – 150 cm^{-1} showing the frequency shift affecting the ω_1 peak with (d) MX100MC00, (e) MX85MC15, and (f) MX80MC20. Zoom in the range of 150 – 550 cm^{-1} showing the changes in ω_2 and ω_6 peaks with (g) MX100MC00, (h) MX85MC15, and (i) MX80MC20.

In Situ EC-AFM. The EC-AFM experiment was performed in a three-electrode configuration, as shown in Figure 1c,f). The $2\text{ mm} \times 5\text{ mm}$ MXene film was used as the sample and entirely fixed on the base using double-sided tape. The electrical connection was made using a thin strip of carbon paper, which was verified by CV before starting each experiment (Figure S4). The approach curve was measured using nonconductive silicon nitride Tip-D (f_0 : 10 – 20 kHz, k : 0.03 N/m). A constant potential (0 , -0.5 , and -1 V vs Ag/AgCl QRE) was applied on the MXene sample, and the approach was terminated when the force reached 1.5 nN. For imaging, the same tip was approached with the sample at an open circuit potential; then, the images were recorded in an area of $40\text{ }\mu\text{m} \times 40\text{ }\mu\text{m}$ with different potentials of the sample (0 , -0.25 , -0.5 , -7.5 , and -1 V vs Ag/AgCl QRE).

RESULTS AND DISCUSSION

The chemical and structural changes of MXene upon application of the potential are analyzed by Raman spectroscopy. From Figure 2a–c, it is seen that all the samples show similar peaks in the range of 100 – 800 cm^{-1} . These peaks can be assigned to different vibration modes (Table 1) as described in the literature.^{69–71} The A_{1g} peak corresponds to in-plane vibrational modes, and the E_g peak is associated with out-of-plane vibrational modes. Note that ω_1 and ω_6 peaks are only visible using a 785 nm excitation laser. The peak at 980 cm^{-1} is related to the electrolyte (SO_4^{2-}), which is thus absent in dry samples. The intensity of SO_4^{2-} remains constant after applying different potentials. This ensures that there is no

Table 1. Assignment of Raman Peaks of MXene in the Range of 100 – 800 cm^{-1}

| Peak assignment | Associated frequency (cm^{-1}) | Vibration mode |
|-----------------|---|---|
| ω_1 | 122 | plasmonic resonance/ $E_g(\text{Ti},\text{C})$ |
| ω_2 | 200 | $A_{1g}(\text{Ti},\text{C},\text{O})$ |
| ω_3 | 730 | $A_{1g}(\text{C})$ |
| ω_4 | 620 | $E_g(\text{C})$ |
| ω_5 | 280 | $E_g(\text{Ti},\text{C},(\text{OH})_2)$ |
| ω_6 | 510 | $A_{1g}(\text{Ti},\text{C},(\text{OH})_2)$ |
| ω_7 | 430 | $E_g(\text{Ti},\text{C},(\text{OH})_2)$ |

drift in the signal, and the quality of measurement is well controlled.

Two major changes are observed on MXene samples when the potential is shifted from 0 to -1 V vs Ag/AgCl QRE. First, the ω_1 peak ($E_g(\text{Ti},\text{C})$) shows a blue shift as compared to the dry samples (Figure 2d–f). For neat MXene, the shift is ca. 4 cm^{-1} , whereas for methylcellulose-functionalized samples it is more pronounced (ca. 4.8 cm^{-1} for MX85MC15 and 5 cm^{-1} for MX80MC20, respectively). This may suggest more freedom in the in-plane $E_g(\text{Ti},\text{C})$ movement as a result of functionalization. Second, the ω_2 ($A_{1g}(\text{Ti},\text{C},\text{O})$) and ω_6 ($A_{1g}(\text{Ti},\text{C},(\text{OH})_2)$) peaks gradually weaken upon applying cathodic potential (Figure 2g–i). This is likely related to the intercalation of Li^+ ions in the MXene films. The interaction of Li^+ ions with $-\text{O}$ in the ω_2 peak and with $-\text{OH}$ in the ω_6 peak

limits the vibrations of these surface groups.^{72,73} The overall increase in the intensity of the spectra might be related to the flake decoupling due to the high Li^+ flux inside the layers at a negative potential. The interlayer interactions become weak after insertion of Li^+ ions that strengthens the out-of-plane vibrations in the 230–470 cm^{-1} and 550–700 cm^{-1} regions. Similarly, a significant increase is observed in ω_3 ($\text{A}_{1g}(\text{C})$) with more applied negative potential.⁶⁹

In the Raman experiments, apart from the chemical structural changes shown in the spectra, we also clearly observed macroscopic deformation of the films upon applying potential. This makes the readjustment of the optical focus indispensable for each measurement. In order to measure this deformation, scanning electrochemical microscopy (SECM) is applied in feedback mode (Figure 3a). Considering that the

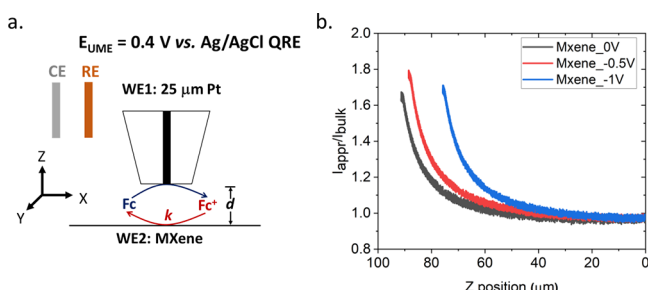


Figure 3. (a) SECM mechanism and (b) approach curves on the MXene surface (MX100MC00) with different potentials applied to the tip (0, −0.5 and −1 V vs Ag/AgCl QRE).

actuation of MXene occurs in the range of 0 to −1 V vs Ag/AgCl QRE, ferrocenedimethanol with a formal potential of 0.4 V vs Ag/AgCl QRE is chosen as a redox probe to ensure fast and full electrochemical regeneration on the MXene sample. In this way, the feedback current measured at the microelectrode depends only on the distance of the tip from the MXene sample and reflects quantitatively the deformation of the sample. Figure 3b shows the approach curves of the Pt microelectrode (0.4 V vs Ag/AgCl QRE) to the two ended fixed neat MXene sample with different applied potentials (0, −0.5 and −1 V vs Ag/AgCl QRE). We emphasize that the approaching starts at exactly the same position in (x , y , z) for the microelectrode. Positive feedback is seen for all three curves, but the current starts to increase and reaches the same value (e.g., 1.5 normalized to the bulk) at different z positions.

This is caused by the deformation of the MXene film upon applying cathodic potential.

To obtain an overview of the actuation performance of the samples, approach curves are measured at different lateral positions between two fixation points with $\Delta x = 500 \mu\text{m}$, as illustrated in Figure 4a. The approach curves are shown in Figures S5 (MX100MC00), S6 (MX85MC15), and S7 (MX80MC20). As discussed in Figure 3b, the shift of the approach curve at the z position reflects the deformation of the MXene sample. Here, a normalized current of 1.1 is chosen to calculate the relative shift for applied potentials of −0.5 V (Figure 4b) and −1 V (Figure 4c) vs 0 V (vs Ag/AgCl QRE) on the MXene surface for each sampling point. This relative height change is then plotted versus the relative position of the probe in x axis ($x = 0$; intersection of the fixed carbon plate and sample). For all samples, the probe reaches a normalized current of 1.1 at a higher position as a result of volume expansion of MXene under cathodic polarization. Such buckling type bumping is more significant for the methylcellulose-functionalized films than that for neat MXene. Taking the highest point of deformation which is at around the middle point between two fixation points, it can be seen that at −0.5 V (vs Ag/AgCl QRE), MX85MC15 and MX80MC20 samples have a deflection of ~52 and ~38 μm, respectively, which is much higher than that of neat MXene (~5.5 μm). At −1 V (vs Ag/AgCl QRE), MX85MC15 and MX80MC20 samples deformed by ~82 and ~76 μm, respectively, whereas the neat MXene film only have ~25 μm deformation. Considering that all the samples have the same geometrical dimensions, one may conclude that the methylcellulose-functionalized MXene has more actuation upon applying cathodic potential, which agrees with our previous observations.⁵⁶

An advantage of SECM is that it can be used not only for characterizing the steady state behavior but also for studying the dynamic actuation of MXene samples. Indeed, the potential applied to MXene can be scanned at different rates while measuring the current response of both the microelectrode and the sample. Technically, this requires switching the connections, i.e., the sample connected as WE1 and the microelectrode connected at WE2. All of the measurements were carried out with the microelectrode positioned near the center (2500 μm) between two fixation points. The experimental configuration is illustrated in Figure 5a. Figure 5b shows the current response from the sample between 0 and −1 V (vs Ag/AgCl QRE) at different scan rates from 5 to 2000 mV/s. As the scan rate increases, the current generally

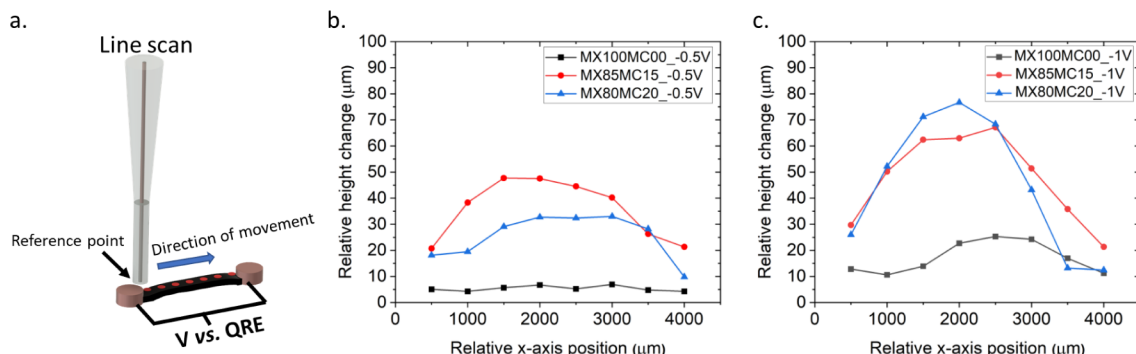


Figure 4. (a) Principle of line scan over MXene surfaces (MX100MC00, MX85MC15, and MX80MC20) and relative deformations at (b) −0.5 V and (c) −1 V with respect to 0 V vs Ag/AgCl QRE.

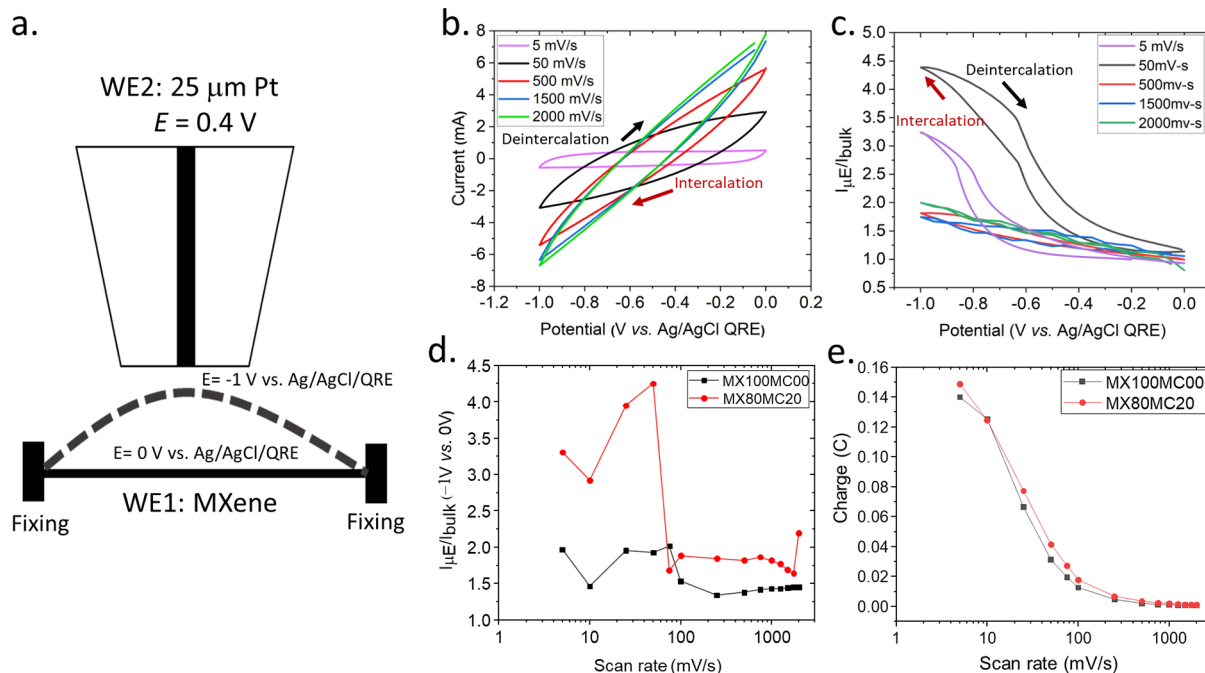


Figure 5. (a) Principle of transient behavior analysis, (b) cyclic voltammetry of the MX80MC20 sample at different scan rates, (c) simultaneous current responses of the Pt microelectrode (I_E) measured over MX80MC20, (d) frequency responses extracted from the experiments performed with MX100MC00 and MX80MC20, and (e) capacitive charge of MX100MC00 and MX80MC20 as a function of the scan rate.

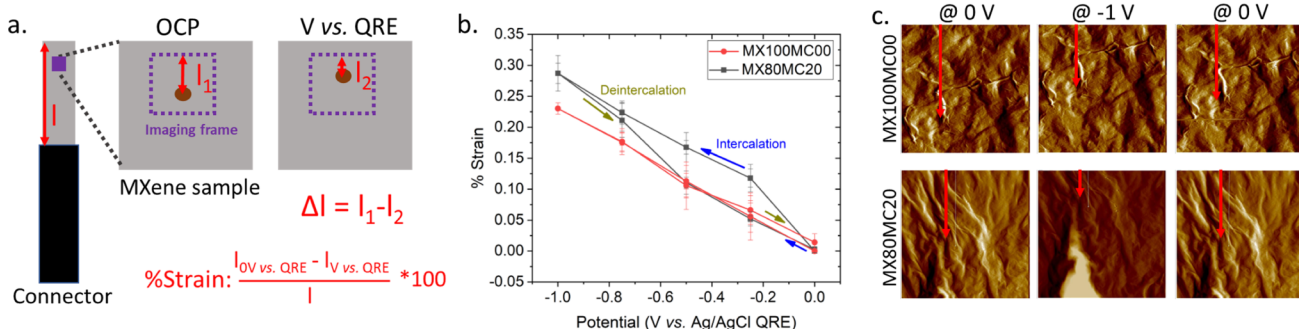


Figure 6. (a) Principle of EC-AFM imaging done at different applied potentials, (b) percentage of strain variation in MX100M00 and MX80M20 samples at 0, -0.25, -0.5, -0.75, and -1 V vs Ag/AgCl QRE, and (c) AFM imaging of MX100M00 and MX80M20 samples at the OCP, 0, -1, and -0.25 V vs Ag/AgCl QRE. Error bar represents the standard deviation of 3 cycles.

increases due to the capacitive effect, but the resistance is also more significant. Meanwhile, the current from the microelectrode is also recorded and normalized by the diffusion limit current of the same electrode in the bulk solution (Figure 5c). As discussed before, this normalized current reflects the distance between the microelectrode and the sample, like in the approach curve of SECM.⁷⁴ Higher current indicates that the sample is closer to the microelectrode and vice versa. Since the microelectrode position is always fixed, this is an indication of dynamic actuation of the sample. It is seen that as the potential of MXene gets negative, the current on the microelectrode increases, suggesting that the MXene expands closer to the microelectrode. During the reverse scan, it contracts away from the microelectrode. The contraction appears to be faster than expansion, as seen from the hysteresis with generally lower current. Moreover, the actuation is more significant at low potential scan rates of the sample, as supported by higher current response on the microelectrode. Figure 5d compares the dynamic actuation behavior of methylcellulose-functionalized and neat MXene. In general,

the methylcellulose-functionalized sample show higher actuation than the nonfunctionalized one. For both samples, the actuation is more significant at lower scan rates, especially at <50 mV/s (<25 mHz). This can be explained by having more time for Li⁺ ions to intercalate in the sample, which is in line with the charge decreasing as the scan rate increases (Figure 5e). The performance measured by SECM is also consistent with that measured at the macroscale, where the strain decreases from 0.541% at 4 mV/s to 0.298% at 40 mV/s for methylcellulose-functionalized MXene, still generally higher than that for neat MXene (0.162% at 4 mV/s and 0.037% at 40 mV/s).⁵⁶

Note that the exact conversion of the microelectrode current to the microelectrode-sample distance has not yet been quantified. This is because the MXene sample especially after intercalation of Li⁺ ions cannot be simply regarded as a planar electrode. First, the sample is rough as seen from the SEM images (Figure S8a,c) and profilometry (Figure S1d-f), and the roughness measured with profilometry is not negligible as compared to the microelectrode-sample distance. Second, the

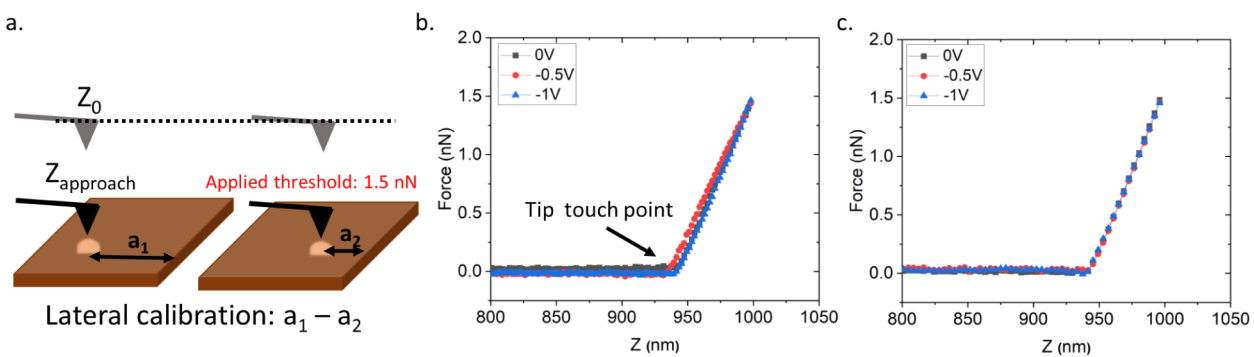


Figure 7. (a) Principle of approach curves on the samples. Approach curve analysis on (b) MX100MC00 and (c) MX80MC20 samples.

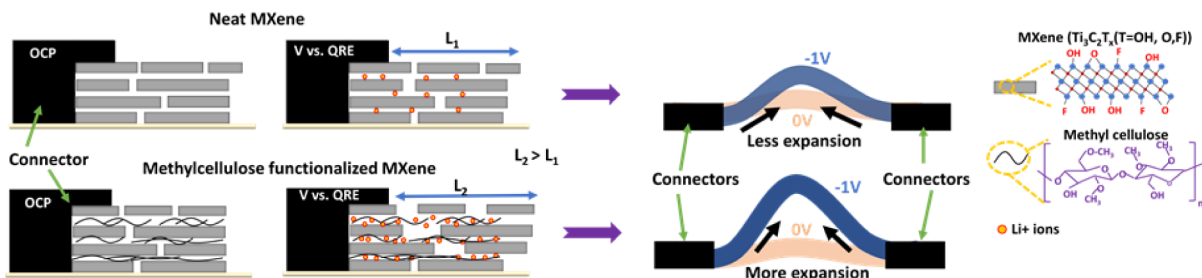


Figure 8. Illustration of the in-plane and buckling type actuation of MXene samples.

buckling type actuation would make the sample locally tilted. This might be a reason for the saturation of current in some approach curves observed in the experiments (Figure S7e). All these factors make the classical SECM approach curve fitting based on planar electrodes invalid, even though the kinetic effect can be reasonably neglected in our experiments considering that the potential applied on MXene is always much lower than the formal potential of ferrocenedimethanol (by at least 0.4 V). Therefore, in Figure 5c, we plot the curves with normalized current and use it as a qualitative measure for comparison. Another point of attention is that the microelectrode current is more sensitive to the distance when it is high or, in other words, when the microelectrode is close to the sample. This nonlinear relationship between the normalized current and distance makes it not meaningful to over-explain the difference in the normalized current in shown Figure 5d.

The above results of SECM address the bucking type actuation of MXene films, which is a mixed effect of in-plane and out-of-plane deformations of the sample. In order to separate the analysis of the two effects, atomic force microscopy (AFM) was performed with a different configuration for fixing the MXene samples. Here, the whole sample is adhered to the base, and the electrical connection is made only at one end. In this way, the out-of-plane deformation could be measured from the touching position of the tip, while the in-plane deformation could be seen from lateral shift of topography images, as illustrated in Figure 6a. Since the measurement position and area ($40 \mu\text{m} \times 40 \mu\text{m}$) are fixed, the lateral shift of the image corresponds to the lateral movement of the sample surface. In practice, this is quantified by the distance between a characteristic feature and the top frame of the image, and the change is relative to the image measured at 0 V applied potential. Figure 6c shows that upon applying the cathodic potential, the flakes move away from the electric connection, indicating that the sample has in-plane expansion. This change is more pronounced for methylcel-

lose-functionalized MXene (MX80M20) as compared to the neat MXene sample (MX100M00) (Figure 6b).

These results also enable calculating the in-plane strain of the samples knowing the length of the sample (Figure S9). It is expressed as $\Delta l/l * 100$, where l represents the length from the monitored point to the fixed end and Δl is the relative displacement of the flake as shown in Figure 6a. Figure 6b shows that the strain is almost linear to the applied potential and is highly reversible upon multiple scans. The MX80MC20 sample shows more strain generation as compared to MX100MC00. Also, the hysteresis type of behavior is seen in MX80MC20 that indicates that below -0.5 V applied potential, the deintercalation step follows the same behavior as MX100MC00.

Apart from in-plane displacement, as shown in Figure 6, AFM was also used to measure the out-of-plane actuation of MXene. The probe always approaches the sample from a fixed Z_0 , and then, the point of contact as evaluated from the approach curve would reflect the vertical displacement of the sample. However, one has to remember that the sample also has in-plane displacement; therefore, it is essential to make sure that the analysis corresponds to the same lateral position on the sample, so that the heterogeneity in topography would not interfere the interpretation. To achieve this goal, the approach curve mapping was done over $20 \mu\text{m} \times 20 \mu\text{m}$ area (256 approach curves per sample). In actuated states, the lateral displacement was first evaluated in the same way as that in Figure 6. This value is then taken for lateral calibration ($X, \Delta Y$). The X value is not changing because the surface was scanned in the center of the width direction. For example, the pixel number (02, 04) at 0 V vs QRE corresponds to the pixel number (02, 08) at -0.5 V vs QRE and the pixel number (02, 12) at -1 V vs QRE (MX100MC00). The detailed illustration is shown in Figures S10 and S11. It is seen that for both MX100MC00 and MX80MC20 samples, there is no significant

change in the touching Z position, indicating that the out-of-plane actuation is insignificant (**Figure 7**).

Following the aforementioned results, the mechanism of MXene actuation is explained in **Figure 8**. The basic principle follows the intercalation/deintercalation of Li^+ ions upon the application of potential. DFT calculations show that the Li^+ ion adsorbs on the oxygen (O (1)) atom surface by maintaining the distance of around $\sim 1.931 \text{ \AA}$ and generates strain in the MXene structure. The $\text{Ti}(1)-\text{O}(1)$ bond interacting with the Li^+ ion showed the maximum expansion with the change in the bond length from 1.964 to 2.226 \AA ($\sim 0.1334\%$ strain). This is in agreement with experimental observations in SECM and AFM. The details about the calculations are provided in the **Supporting Information** (**Table S1** and **Figure S12**).

The neat MXene shows less in-plane expansion and thus less strain than methylcellulose-functionalized samples, as supported by the Raman and AFM results. This could be because of the presence of a polymer that may weaken the interlayer interaction and may allow larger in-plane sliding of MXene sheets, as discussed in previous work.⁵⁸ However, in the case of buckling type actuation measured by SECM, this enhanced in-plane actuation may yield more significant apparent out-of-plane deformation of the sample for functionalized samples.

CONCLUSION

In this work, we characterized the electrochemical actuation of functionalized MXene films through *in situ* techniques at the microscale. First, Raman spectroscopy was used to study the chemical structural changes happening in MXene films upon the reversible intercalation/deintercalation of ions. It was seen that the increase in methylcellulose functionalization results in high in-plane-vibrations ($\omega_1: E_g(\text{Ti},\text{C})$) at the applied cathodic potential. The out-of-plane vibrations (ω_2 and ω_6) showed suppression in peak intensities due to the interaction of Li^+ ions with the $-\text{O}$ and $-\text{OH}$ terminal groups. This interlayer decoupling resulted in an increase in the intensity at other wavelengths of the spectra. Second, the buckling type deformation of MXene samples was studied by scanning electrochemical microscopy (SECM). The line scan between two fixations of the sample helped in understanding the role of functionalization for this deformation. It was seen that 20 and 15% methylcellulose-functionalized samples showed the highest deformation of ~ 82 and $\sim 76 \mu\text{m}$ at -1 V (vs Ag/AgCl QRE) compared to neat MXene ($\sim 25 \mu\text{m}$). Further dynamic behavior studies by SECM showed that samples undergo significant cyclic expansion/contraction actuation at low scan rates ($<50 \text{ mV/s}$). Furthermore, AFM imaging and approach curve analysis helped to analyze this expansion/contraction in more details. It was seen that both neat and methylcellulose-functionalized samples undergo mainly in-plane deformation. This deformation is more significant in the case of functionalized samples that leads to more strain generation and results in high actuation.

ASSOCIATED CONTENT

Supporting Information

The Supporting Information is available free of charge at <https://pubs.acs.org/doi/10.1021/acs.chemmater.4c01597>.

Data including the experiments of profilometry, cyclic voltammetry of microelectrode and MXene samples, Raman experiments, SECM approach curves, AFM imaging and approach curves, and DFT calculations of

the structure of MXene before and after intercalation of Li^+ ions (**PDF**)

Videos of AFM imaging at different potentials of pure MXene (**MP4**)

MXene functionalized with 20% methylcellulose (**MP4**)

AUTHOR INFORMATION

Corresponding Authors

Liang Liu — Université de Lorraine, Nancy 54000, France;
ORCID: [0000-0002-8396-0554](https://orcid.org/0000-0002-8396-0554); Email: liang.liu@cnrs.fr

Mathieu Etienne — Université de Lorraine, Nancy 54000, France; ORCID: [0000-0003-3166-4072](https://orcid.org/0000-0003-3166-4072); Email: mathieu.etienne@cnrs.fr

Authors

Harpreet Singh — Université de Lorraine, Nancy 54000, France

Shaohua Chen — School of Materials Science and Engineering, Nanyang Technological University, Singapore 639798, Singapore; ORCID: [0000-0002-0076-2561](https://orcid.org/0000-0002-0076-2561)

Grégoire Francius — Université de Lorraine, Nancy 54000, France; ORCID: [0000-0001-8533-9449](https://orcid.org/0000-0001-8533-9449)

Pooi See Lee — School of Materials Science and Engineering, Nanyang Technological University, Singapore 639798, Singapore; ORCID: [0000-0003-1383-1623](https://orcid.org/0000-0003-1383-1623)

Complete contact information is available at:

<https://pubs.acs.org/10.1021/acs.chemmater.4c01597>

Author Contributions

The manuscript was written through contributions of all authors. All authors have given approval to the final version of the manuscript.

Funding

This work is funded by the National Research Foundation of Singapore under project no. NRF2020-NRF-ANR102 MEACT (ANR-20-CE09-0028). This research was also supported by the DrEAM program under the Lorraine Université d'Excellence Initiative (LUE) for international mobility of its PhD students.

Notes

The authors declare no competing financial interest.

ACKNOWLEDGMENTS

The platform of spectroscopy and microscopy of interfaces (SMI) of LCPME is acknowledged. Dr Manuel Dossot and Dr Jérôme Grausem are acknowledged for the training and technical support for Raman spectroscopy. Dr Mariela Alicia Brites Helú is acknowledged for SEM measurements.

ABBREVIATIONS

EC-AFM electrochemical atomic force microscopy

SECM scanning electrochemical microscopy

CV cyclic voltammetry

QRE quasi-reference electrode

REFERENCES

- (1) Zhou, J.; Mulle, M.; Zhang, Y.; Xu, X.; Li, E. Q.; Han, F.; Thoroddsen, S. T.; Lubineau, G. High-Ampacity Conductive Polymer Microfibers as Fast Response Wearable Heaters and Electro-mechanical Actuators. *J. Mater. Chem. C Mater.* **2016**, *4* (6), 1238–1249.

- (2) Yang, Z.; Zhang, L. Magnetic Actuation Systems for Miniature Robots: A Review. *Adv. Intell. Syst.* **2020**, 2 (9), 2000082.
- (3) Gural'skiy, I. A.; Quintero, C. M.; Costa, J. S.; Demont, P.; Molnár, G.; Salmon, L.; Shepherd, H. J.; Bousseksou, A. Spin Crossover Composite Materials for Electrothermomechanical Actuators. *J. Mater. Chem. C* **2014**, 2 (16), 2949–2955.
- (4) Ze, Q.; Kuang, X.; Wu, S.; Wong, J.; Montgomery, S. M.; Zhang, R.; Kovitz, J. M.; Yang, F.; Qi, H. J.; Zhao, R. Magnetic Shape Memory Polymers with Integrated Multifunctional Shape Manipulation. *Adv. Mater.* **2020**, 32 (4), 1906657.
- (5) Mohith, S.; Upadhyay, A. R.; Navin, K. P.; Kulkarni, S. M.; Rao, M. Recent Trends in Piezoelectric Actuators for Precision Motion and Their Applications: A Review. *Smart Mater. Struct.* **2021**, 30 (1), 013002.
- (6) Priimagi, A.; Barrett, C. J.; Shishido, A. Recent Twists in Photoactuation and Photoalignment Control. *J. Mater. Chem. C* **2014**, 2 (35), 7155–7162.
- (7) Yu, L.; Cheng, Z.; Dong, Z.; Zhang, Y.; Yu, H. Photomechanical Response of Polymer-Dispersed Liquid Crystals/Graphene Oxide Nanocomposites. *J. Mater. Chem. C* **2014**, 2 (40), 8501–8506.
- (8) Hua, D.; Zhang, X.; Ji, Z.; Yan, C.; Yu, B.; Li, Y.; Wang, X.; Zhou, F. 3D Printing of Shape Changing Composites for Constructing Flexible Paper-Based Photothermal Bilayer Actuators. *J. Mater. Chem. C Mater.* **2018**, 6 (8), 2123–2131.
- (9) Oh, J.; Kozlov, M. E.; Carretero-González, J.; Castillo-Martínez, E.; Baughman, R. H. Thermal Actuation of Graphene Oxide Nanoribbon Mats. *Chem. Phys. Lett.* **2011**, 505 (1–3), 31–36.
- (10) Neagu, C. R. A Medical Microactuator Based On An Electrochemical Principle. Ph.D Thesis; University of Twente, 1998.
- (11) Nakshatharan, S. S.; Vunder, V.; Pöldsalu, I.; Johanson, U.; Punning, A.; Aabloo, A. Modelling and Control of Ionic Electroactive Polymer Actuators under Varying Humidity Conditions. *Actuators* **2018**, 7 (1), 7.
- (12) Deng, Q.; Jia, H.; An, C.; Wu, S.; Zhao, S.; Hu, N. Progress and Prospective of Electrochemical Actuator Materials. *Compos. Part A Appl. Sci. Manuf.* **2023**, 165, 107336.
- (13) Bar-Cohen, Y. *Electroactive Polymer (EAP) Actuators As Artificial Muscles: reality, Potential, And Challenges*; SPIE Digital Library, 2004, 136.
- (14) O'Halloran, A.; O'Malley, F.; McHugh, P. A Review on Dielectric Elastomer Actuators, Technology, Applications, and Challenges. *J. Appl. Phys.* **2008**, 104 (7), 071101.
- (15) Li, W.; Li, F.; Li, H.; Su, M.; Gao, M.; Li, Y.; Su, D.; Zhang, X.; Song, Y. Flexible Circuits and Soft Actuators by Printing Assembly of Graphene. *ACS Appl. Mater. Interfaces* **2016**, 8 (19), 12369–12376.
- (16) Deng, H.; Zhang, C.; Su, J.-W.; Xie, Y.; Zhang, C.; Lin, J. Bioinspired Multi-Responsive Soft Actuators Controlled by Laser Tailored Graphene Structures. *J. Mater. Chem. B* **2018**, 6 (34), 5415–5423.
- (17) Zhu, S.-E.; Shabani, R.; Rho, J.; Kim, Y.; Hong, B. H.; Ahn, J.-H.; Cho, H. J. Graphene-Based Bimorph Microactuators. *Nano Lett.* **2011**, 11 (3), 977–981.
- (18) Aliev, A. E.; Oh, J.; Kozlov, M. E.; Kuznetsov, A. A.; Fang, S.; Fonseca, A. F.; Ovalle, R.; Lima, M. D.; Haque, M. H.; Gartstein, Y. N.; et al. Giant-Stroke Superelastic Carbon Nanotube Aerogel Muscles. *Science* **2009**, 323 (5921), 1575–1578.
- (19) Brochu, P.; Pei, Q. Dielectric Elastomers for Actuators and Artificial Muscles. In *Electroactivity in Polymeric Materials*; Springer US: Boston, MA, 2012; pp. 156.
- (20) Zhao, Y.; Song, L.; Zhang, Z.; Qu, L. Stimulus-Responsive Graphene Systems towards Actuator Applications. *Energy Environ. Sci.* **2013**, 6 (12), 3520.
- (21) Zhang, Y.-L.; Li, J.-C.; Zhou, H.; Liu, Y.-Q.; Han, D.-D.; Sun, H.-B. Electro-Responsive Actuators Based on Graphene. *The Innovation* **2021**, 2 (4), 100168.
- (22) Xie, X.; Qu, L.; Zhou, C.; Li, Y.; Zhu, J.; Bai, H.; Shi, G.; Dai, L. An Asymmetrically Surface-Modified Graphene Film Electrochemical Actuator. *ACS Nano* **2010**, 4 (10), 6050–6054.
- (23) Weng, M.; Ding, M.; Zhou, P.; Ye, Y.; Luo, Z.; Ye, X.; Guo, Q.; Chen, L. Multi-Functional and Integrated Actuators Made with Bio-Inspired Cobweb Carbon Nanotube–Polymer Composites. *Chem. Eng. J.* **2023**, 452, 139146.
- (24) Yang, X.; Miao, M. Carbon Nanotube Yarn-Based Actuators. In *Carbon Nanotube Fibers and Yarns*; Elsevier, 2020; pp. 271291.
- (25) Goswami, S. K.; McAdam, C. J.; Lee, A. M. M.; Hanton, L. R.; Moratti, S. C. Linear Electrochemical Actuators with Very Large Strains Using Carbon Nanotube-Redox Gel Composites. *J. Mater. Chem. A Mater.* **2013**, 1 (10), 3415.
- (26) Li, Q.; Wu, J.-T.; Liu, Y.; Qi, X.-M.; Jin, H.-G.; Yang, C.; Liu, J.; Li, G.-L.; He, Q.-G. Recent Advances in Black Phosphorus-Based Electrochemical Sensors: A Review. *Anal. Chim. Acta* **2021**, 1170, 338480.
- (27) Lu, C.; Yang, Y.; Wang, J.; Fu, R.; Zhao, X.; Zhao, L.; Ming, Y.; Hu, Y.; Lin, H.; Tao, X.; et al. High-Performance Graphdiyne-Based Electrochemical Actuators. *Nat. Commun.* **2018**, 9 (1), 752.
- (28) Lu, F.; Xiang, K.; Wang, Y.; Chen, T. Electrochemical Actuators Based on Nitrogen-Doped Carbons Derived from Zeolitic Imidazolate Frameworks. *Mater. Des.* **2020**, 187, 108405.
- (29) Shi, Y.-X.; Wu, Y.; Wang, S.-Q.; Zhao, Y.-Y.; Li, T.; Yang, X.-Q.; Zhang, T. Soft Electrochemical Actuators with a Two-Dimensional Conductive Metal–Organic Framework Nanowire Array. *J. Am. Chem. Soc.* **2021**, 143 (10), 4017–4023.
- (30) Hung, N. T.; Nugraha, A. R. T.; Saito, R. Two-Dimensional MoS₂ Electromechanical Actuators. *J. Phys. D: appl. Phys.* **2018**, 51 (7), 075306.
- (31) 2D Metal Carbides and Nitrides (MXenes); Anasori, B.; Gogotsi, Y., Eds.; Springer International Publishing: Cham, 2019.
- (32) Zhang, J.; Kong, N.; Uzun, S.; Levitt, A.; Seyedin, S.; Lynch, P. A.; Qin, S.; Han, M.; Yang, W.; Liu, J.; et al. Scalable Manufacturing of Free-Standing, Strong Ti₃C₂T_x MXene Films with Outstanding Conductivity. *Adv. Mater.* **2020**, 32 (23), 2001093.
- (33) Lipatov, A.; Lu, H.; Alhabeb, M.; Anasori, B.; Gruverman, A.; Gogotsi, Y.; Sinitskii, A. Elastic Properties of 2D Ti₃C₂T_x MXene Monolayers and Bilayers. *Sci. Adv.* **2018**, 4 (6), No. eaat0491.
- (34) Hart, J. L.; Hantanasirisakul, K.; Lang, A. C.; Anasori, B.; Pinto, D.; Pivak, Y.; van Omme, J. T.; May, S. J.; Gogotsi, Y.; Taheri, M. L. Control of MXenes' Electronic Properties through Termination and Intercalation. *Nat. Commun.* **2019**, 10 (1), 522.
- (35) Liang, X.; Garsuch, A.; Nazar, L. F. Sulfur Cathodes Based on Conductive MXene Nanosheets for High-Performance Lithium–Sulfur Batteries. *Angew. Chem., Int. Ed.* **2015**, 54 (13), 3907–3911.
- (36) Alhabeb, M.; Maleski, K.; Anasori, B.; Lelyukh, P.; Clark, L.; Sin, S.; Gogotsi, Y. Guidelines for Synthesis and Processing of Two-Dimensional Titanium Carbide (Ti₃C₂T_x MXene). *Chem. Mater.* **2017**, 29 (18), 7633–7644.
- (37) Mashtalar, O.; Lukatskaya, M. R.; Zhao, M.; Barsoum, M. W.; Gogotsi, Y. Amine-Assisted Delamination of Nb₂C MXene for Li-Ion Energy Storage Devices. *Adv. Mater.* **2015**, 27 (23), 3501–3506.
- (38) Lipatov, A.; Alhabeb, M.; Lu, H.; Zhao, S.; Loes, M. J.; Vorobeva, N. S.; Dall'agnese, Y.; Gao, Y.; Gruverman, A.; Gogotsi, Y.; et al. Electrical and Elastic Properties of Individual Single-Layer Nb₄C₃T_x MXene Flakes. *Adv. Electron. Mater.* **2020**, 6 (4), 1901382.
- (39) Zhao, S.; Chen, C.; Zhao, X.; Chu, X.; Du, F.; Chen, G.; Gogotsi, Y.; Gao, Y.; Dall'agnese, Y. Flexible Nb₄C₃T_x Film with Large Interlayer Spacing for High-Performance Supercapacitors. *Adv. Funct. Mater.* **2020**, 30 (47), 2000815.
- (40) Shan, Q.; Mu, X.; Alhabeb, M.; Shuck, C. E.; Pang, D.; Zhao, X.; Chu, X.-F.; Wei, Y.; Du, F.; Chen, G.; et al. Two-Dimensional Vanadium Carbide (V₂C) MXene as Electrode for Supercapacitors with Aqueous Electrolytes. *Electrochim. Commun.* **2018**, 96, 103–107.
- (41) VahidMohammadi, A.; Mojtabavi, M.; Caffrey, N. M.; Wanunu, M.; Beidaghi, M. Assembling 2D MXenes into Highly Stable Pseudocapacitive Electrodes with High Power and Energy Densities. *Adv. Mater.* **2019**, 31 (8), 1806931.
- (42) Zhang, Y.; Lu, W.; Zhou, J.; Sun, D.; Li, H. The Multiple Synthesis of Layered V₂CTx-MXene Composites with Enhanced Electrochemical Properties. *J. Alloys Compd.* **2022**, 929, 167276.

- (43) Halim, J.; Kota, S.; Lukatskaya, M. R.; Naguib, M.; Zhao, M.; Moon, E. J.; Pitock, J.; Nanda, J.; May, S. J.; Gogotsi, Y.; et al. Synthesis and Characterization of 2D Molybdenum Carbide (MXene). *Adv. Funct. Mater.* **2016**, *26* (18), 3118–3127.
- (44) Hussain, I.; Rehman, F.; Saraf, M.; Zhang, T.; Wang, R.; Das, T.; Luo, Z.; Gogotsi, Y.; Zhang, K. Electrochemical Properties of $\text{Mo}_4\text{VC}_4\text{T}_x\text{MXene}$ in Aqueous Electrolytes. *ACS Appl. Mater. Interfaces* **2024**, *16*, 38053.
- (45) Saraf, M.; Chacon, B.; Ippolito, S.; Lord, R. W.; Anayee, M.; Wang, R.; Inman, A.; Shuck, C. E.; Gogotsi, Y. Enhancing Charge Storage of $\text{Mo}_2\text{Ti}_2\text{C}_3$ MXene by Partial Oxidation. *Adv. Funct. Mater.* **2024**, *34* (1), 2306815.
- (46) Jun, B.-M.; Kim, S.; Heo, J.; Park, C. M.; Her, N.; Jang, M.; Huang, Y.; Han, J.; Yoon, Y. Review of MXenes as New Nanomaterials for Energy Storage/Delivery and Selected Environmental Applications. *Nano Res.* **2019**, *12* (3), 471–487.
- (47) Lipatov, A.; Goad, A.; Loes, M. J.; Vorobeva, N. S.; Abourahma, J.; Gogotsi, Y.; Sinitzkii, A. High Electrical Conductivity and Breakdown Current Density of Individual Monolayer $\text{Ti}_3\text{C}_2\text{T}$ MXene Flakes. *Matter* **2021**, *4* (4), 1413–1427.
- (48) Ying, G.; Kota, S.; Dillon, A. D.; Fafarman, A. T.; Barsoum, M. W. Conductive Transparent V 2 CT x (MXene) Films. *FlatChem* **2018**, *8*, 25–30.
- (49) Zhu, K.; Jin, Y.; Du, F.; Gao, S.; Gao, Z.; Meng, X.; Chen, G.; Wei, Y.; Gao, Y. Synthesis of Ti2CT MXene as Electrode Materials for Symmetric Supercapacitor with Capable Volumetric Capacitance. *J. Energy Chem.* **2019**, *31*, 11–18.
- (50) Ghidiu, M.; Lukatskaya, M. R.; Zhao, M.-Q.; Gogotsi, Y.; Barsoum, M. W. Conductive Two-Dimensional Titanium Carbide ‘Clay’ with High Volumetric Capacitance. *Nature* **2014**, *516* (7529), 78–81.
- (51) Ling, Z.; Ren, C. E.; Zhao, M.-Q.; Yang, J.; Giamarco, J. M.; Qiu, J.; Barsoum, M. W.; Gogotsi, Y. Flexible and Conductive MXene Films and Nanocomposites with High Capacitance. *Proc. Natl. Acad. Sci. U. S. A.* **2014**, *111* (47), 16676–16681.
- (52) Khanal, R.; Irle, S. Effect of Surface Functional Groups on MXene Conductivity. *J. Chem. Phys.* **2023**, *158* (19), 194701.
- (53) Berdiyorov, G. R.; Mahmoud, K. A. Effect of Surface Termination on Ion Intercalation Selectivity of Bilayer $\text{Ti}_3\text{C}_2\text{T}_2$ ($\text{T} = \text{F}, \text{O}$ and OH) MXene. *Appl. Surf. Sci.* **2017**, *416*, 725–730.
- (54) Tang, Q.; Zhou, Z.; Shen, P. Are MXenes Promising Anode Materials for Li Ion Batteries? Computational Studies on Electronic Properties and Li Storage Capability of Ti_3C_2 and $\text{Ti}_3\text{C}_2\text{X}_2$ ($\text{X} = \text{F}, \text{OH}$) Monolayer. *J. Am. Chem. Soc.* **2012**, *134* (40), 16909–16916.
- (55) Yang, Q.; Eder, S. J.; Martini, A.; Grützmacher, P. G. Effect of Surface Termination on the Balance between Friction and Failure of $\text{Ti}_3\text{C}_2\text{Tx}$ MXenes. *NPJ. Mater. Degrad.* **2023**, *7* (1), 6.
- (56) Chen, S.; Ciou, J.; Yu, F.; Chen, J.; Lv, J.; Lee, P. S. Molecular-Level Methylcellulose/MXene Hybrids with Greatly Enhanced Electrochemical Actuation. *Adv. Mater.* **2022**, *34* (29), 2200660.
- (57) Liu, L.; Wang, C.; Wu, Z.; Xing, Y. Ultralow-Voltage-Driven Artificial Muscles Based on a 3D Structure MXene-PEDOT: PSS/AgNWs Electrode. *ACS Appl. Mater. Interfaces* **2022**, *14* (16), 18150–18158.
- (58) Wang, T.; Wang, T.; Weng, C.; Liu, L.; Zhao, J.; Zhang, Z. Engineering Electrochemical Actuators with Large Bending Strain Based on 3D-Structure Titanium Carbide MXene Composites. *Nano Res.* **2021**, *14* (7), 2277–2284.
- (59) Chen, S.; Tan, S. F.; Singh, H.; Liu, L.; Etienne, M.; Lee, P. S. Functionalized MXene Films with Substantially Improved Low-Voltage Actuation. *Adv. Mater.* **2024**, *36* (9), 2307045.
- (60) Baughman, R. H.; Cui, C.; Zakhidov, A. A.; Iqbal, Z.; Barisci, J. N.; Spinks, G. M.; Wallace, G. G.; Mazzoldi, A.; De Rossi, D.; Rinzler, A. G.; et al. Carbon Nanotube Actuators. *Science* **1999**, *284* (5418), 1340–1344.
- (61) Umrao, S.; Tabassian, R.; Kim, J.; Nguyen, V. H.; Zhou, Q.; Nam, S.; Oh, I.-K. MXene Artificial Muscles Based on Ionically Cross-Linked $\text{Ti}_3\text{C}_2\text{T}_x$ Electrode for Kinetic Soft Robotics. *Sci. Rob.* **2019**, *4* (33), No. eaaw7797.
- (62) Zheng, W. Beginner’s Guide to Raman Spectroelectrochemistry for Electrocatalysis Study. *Chem.—methods* **2023**, *3* (2), No. e202200042.
- (63) Moldovan, R.; Vereshchagina, E.; Milenko, K.; Iacob, B.-C.; Bodoki, A. E.; Falamas, A.; Tosa, N.; Muntean, C. M.; Farcău, C.; Bodoki, E. Review on Combining Surface-Enhanced Raman Spectroscopy and Electrochemistry for Analytical Applications. *Anal. Chim. Acta* **2022**, *1209*, 339250.
- (64) Li, L.; Xu, J.; Shi, M.; He, J.; Jiang, J.; Dai, K.; Jiang, Z.; Yan, C. In-Situ Raman Investigation and Application of MXene-Stabilized Polypyrrole Composite for Flexible Aqueous Batteries. *Mater. Des.* **2022**, *217*, 110606.
- (65) Bard, A. J.; Fan, F. R. F.; Kwak, J.; Lev, O. Scanning Electrochemical Microscopy. Introduction and Principles. *Anal. Chem.* **1989**, *61* (2), 132–138.
- (66) Cornut, R.; Lefrou, C. New Analytical Approximation of Feedback Approach Curves with a Microdisk SECM Tip and Irreversible Kinetic Reaction at the Substrate. *J. Electroanal. Chem.* **2008**, *621* (2), 178–184.
- (67) *Scanning Electrochemical Microscopy*, Bard, A. J.; Mirkin, M. V., eds.; CRC Press, 2012.
- (68) Deng, X.; Galli, F.; Koper, M. T. M. In Situ Electrochemical AFM Imaging of a Pt Electrode in Sulfuric Acid under Potential Cycling Conditions. *J. Am. Chem. Soc.* **2018**, *140* (41), 13285–13291.
- (69) Sarycheva, A.; Gogotsi, Y. Raman Spectroscopy Analysis of the Structure and Surface Chemistry of $\text{Ti}_3\text{C}_2\text{T}$ XMXene. *Chem. Mater.* **2020**, *32* (8), 3480–3488.
- (70) Hu, T.; Wang, J.; Zhang, H.; Li, Z.; Hu, M.; Wang, X. Vibrational Properties of Ti_3C_2 and $\text{Ti}_3\text{C}_2\text{T}_2$ ($\text{T} = \text{O}, \text{F}, \text{OH}$) Monosheets by First-Principles Calculations: A Comparative Study. *Phys. Chem. Chem. Phys.* **2015**, *17* (15), 9997–10003.
- (71) Placke, T.; Gonzalez-Julian, J.; Bärmann, P.; Nölle, R.; Siozios, V.; Ruttert, M.; Guillen, O.; Winter, M. Solvent Co-Intercalation into Few-Layered $\text{Ti}_3\text{C}_2\text{Tx}$ Mxenes in Lithium Ion Batteries Induced by Acidic or Basic Post-Treatment. *ACS Nano* **2021**, *15* (2), 3295–3308.
- (72) Come, J.; Black, J. M.; Lukatskaya, M. R.; Naguib, M.; Beidaghi, M.; Rondinone, A. J.; Kalinin, S. V.; Wesolowski, D. J.; Gogotsi, Y.; Balke, N. Controlling the Actuation Properties of MXene Paper Electrodes upon Cation Intercalation. *Nano Energy* **2015**, *17*, 27–35.
- (73) Li, J.; Wang, X.; Sun, W.; Maleski, K.; Shuck, C.E.; Li, K.; Urbankowski, P.; Hantanasisakul, K.; Wang, X.; Gogotsi, Y. Intercalation Induced Reversible Electrochromic Behavior Of Two-Dimensional $\text{Ti}_3\text{C}_2\text{T}_x$ MXene In Organic Electrolytes. *ChemElectroChem* **2020**, *8*, 151–156.
- (74) Santana, J. J.; Izquierdo, J.; Souto, R. M. Uses of Scanning Electrochemical Microscopy (SECM) for the Characterization with Spatial and Chemical Resolution of Thin Surface Layers and Coating Systems Applied on Metals: A Review. *Coatings* **2022**, *12* (5), 637.